A new functional form to study the solar wind control of the magnetopause size and shape

J.-H. Shue,[1,2] J.K. Chao,[1,3] H.C. Fu,[1] C.T. Russell,[4] P. Song,[5,6]
K.K. Khurana,[4] and H.J. Singer[7]

Abstract. In this study a new functional form, $r = r_0[2/(1+\cos\theta)]^\alpha$, is used to fit the size and shape of the magnetopause using crossings from ISEE 1 and 2, Active Magnetospheric Particle Tracer Explorers/Ion Release Module (AMPTE/IRM), and IMP 8 satellites. This functional form has two parameters, r_0 and α, representing the standoff distance and the level of tail flaring. The value r is the radial distance at an angle (θ) between the Sun-Earth line and the direction of r. It is found that r_0 varies with the interplanetary magnetic field (IMF) B_z component and has a break in the slope at $B_z = 0$ nT. The best-fit value of r_0 decreases with increasing southward IMF B_z. For northward IMF B_z, the best-fit value of r_0 increases slightly with increasing B_z. The best-fit value of α increases monotonically with decreasing IMF B_z. The dynamic pressure (D_p) also changes r_0 and α. The parameters D_p and r_0 are related by a power law of $-1/(6.6\pm0.8)$. The best-fit value of α is slightly larger for larger dynamic pressure, which implies that D_p also has a role in flux transfer from the dayside to the nightside, but the size of this effect is small. An explicit function for the size and shape of the magnetopause, in terms of D_p and B_z, is obtained by using multiple parameter fitting in a form that is useful for operational space applications such as predicting when satellites at geosynchronous orbit will be found in the magnetosheath.

1. Introduction

The solar wind interacts with the Earth's dipole magnetic field, confining it in a magnetic cavity or magnetosphere with a outer boundary called the magnetopause. The size and shape of the magnetopause can be determined by the dynamic and static pressure of the solar wind and the magnetic pressure of the magnetosphere in the absence of solar wind coupling to the magnetosphere. In this study we use in situ magnetopause crossings and obtain a quantitative relation between the size and shape of the magnetopause and the solar wind parameters, dynamic pressure (D_p), and inter-

planetary magnetic field (IMF) B_z. With this relation, we can predict the size and shape of the magnetopause for given values of IMF B_z and D_p. This relation is useful for space weather operations and can be used for comparisons with numerical simulations or theoretical models.

Various models for the size and shape of the magnetopause have been studied in the past [*Fairfield*, 1971; *Howe and Binsack*, 1972; *Formisano et al.*, 1979; *Sibeck et al.*, 1991; *Petrinec et al.*, 1991; *Petrinec and Russell*, 1993a, 1996; *Roelof and Sibeck*, 1993]. The *Howe and Binsack* [1972] model and the *Petrinec and Russell* [1996] model of the nightside magnetopause used inverse trigonometric functions to describe the magnetopause size and shape. The other models used either the general equation of an ellipsoid with two parameters (eccentricity and standoff distance) or the general quadratic equation. *Fairfield* [1995] discussed the limitations of using an elliptic equation. The ellipse must close at some point on the nightside and hence cannot represent a magnetopause that continues to flare. A new function should have the flexibility to produce a magnetopause which is open or closed. In this paper we present such a new function to fit the size and shape of the magnetopause:

$$r = r_0\left(\frac{2}{1+\cos\theta}\right)^\alpha \tag{1}$$

where r_0 and α are the standoff distance and the level of tail flaring, respectively. The parameter r_0 is the

[1]Institute of Space Science, National Central University, Chungli, Taiwan.
[2]Now at Solar-Terrestrial Environment Laboratory, Nagoya University, Toyokawa, Japan.
[3]Also at High Altitude Observatory, NCAR, Boulder, Colorado.
[4]Institute of Geophysics and Planetary Physics, University of California, Los Angeles.
[5]High Altitude Observatory, NCAR, Boulder, Colorado.
[6]Now at Space Physics Research Laboratory, University of Michigan, Ann Arbor.
[7]NOAA Space Environment Center, Boulder, Colorado.

distance at which balance is achieved between the solar wind dynamic pressure and Earth's dipole magnetic field at the subsolar region. The value r is the radial distance at an angle (θ) between the Earth-Sun line and the direction of r. Unlike the equation of an ellipsoid, this functional form has the flexibility to produce a magnetopause which is closed ($\alpha < 0.5$), asymptotes to a finite tail radius ($\alpha = 0.5$), or expands with increasing distance from the Earth ($\alpha > 0.5$). The behavior of the new function in terms of r_0 and α is shown in Figure 1. The top panel of Figure 1 shows the function for different r_0 values and $\alpha = 0.5$. It can be seen that the curves for different r_0 are self-similar. The bottom panel of Figure 1 shows the function for different values of α and $r_0 = 10\ R_e$, where R_e is Earth radii. It is found that the larger the value of α, the more the tail flares.

In the study by *Petrinec et al.* [1991], an ellipsoid function was used to fit the position of crossings from ISEE 1 and 2 satellites. Since the apogee of ISEE 1 and 2 is 22.5 R_e, their results are limited principally to the dayside. Also, their data were only separated into two bins, southward and northward IMF B_z. *Petrinec*

and Russell [1993a, 1996] extended their model to the magnetotail using a different functional form. This empirical model has a greater parametric extent than the earlier model [*Petrinec et al.*, 1991]. In their study the value of D_p ranges from 0.5 nPa to 8.0 nPa and the value of IMF B_z is for $\geq$ −10 nT. They inferred the position of the magnetopause based on the total pressure balance at the magnetopause, and attached it in a piecewise continuous manner to the dayside model.

Sibeck et al. [1991] assembled a data set of magnetopause crossings from different studies that may have used different selection criteria. They separated the data by IMF B_z without considering the variation of D_p and by D_p without considering the variation of IMF B_z. *Roelof and Sibeck* [1993] improved upon the fit with a method for determining the size and shape of the magnetopause as a bivariate function of hourly averages of IMF B_z and D_p. The coefficients for their functions are rather complicated, so it is not easy to reproduce the size and shape of magnetopause for given IMF B_z and D_p.

In this study different data sets, different assumptions, and a different function than the previous models are used to fit the size and shape of the magnetopause. We also use in situ magnetopause crossings and a single function to determine the size and shape of the magnetopause at both dayside and nightside locations. Also, 5-min average IMF B_z and D_p are used to reflect more precisely the solar wind conditions corresponding to each individual crossing. Moreover, we fit the data simultaneously as a function of D_p and IMF B_z by using a multiple parameter fitting. An explicit function, with simple coefficients, is obtained at the last stage of our analysis.
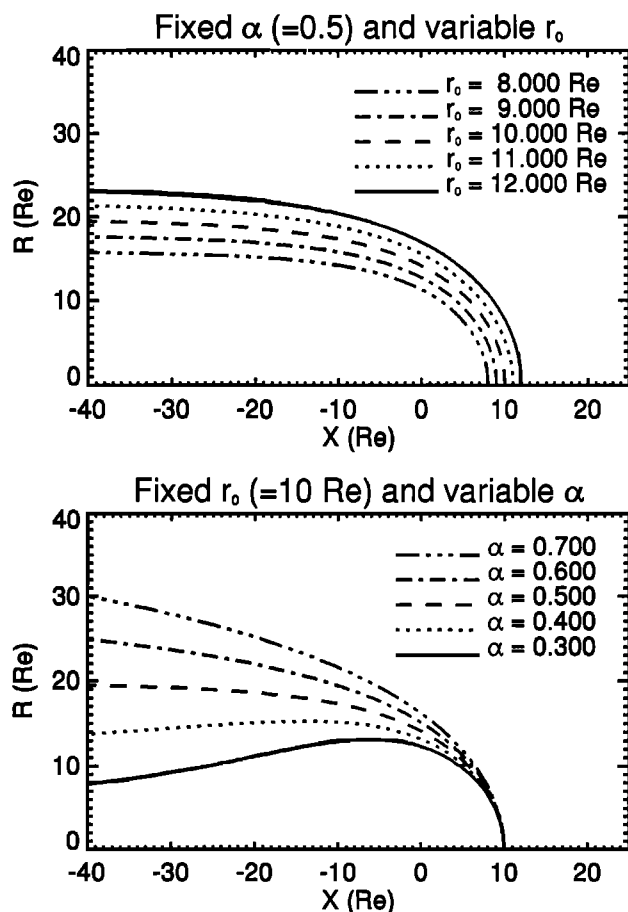
2. Data Preparation

For this investigation we have used data from ISEE 1 and 2; AMPTE/IRM; GOES 2, 5, and 6; IMP 8; and ISEE 3. The orbits of ISEE 1 and 2, AMPTE/IRM, and IMP 8 traverse the magnetopause and can be used to identify the magnetopause crossings. The two satellites, IMP 8 and ISEE 3, are principally in the solar wind and were used to obtain solar wind conditions corresponding to each individual magnetopause crossing. The inclination of ISEE 1 and 2 satellites were initially 30°, with a perigee of 1.5 R_e and an apogee of 22.5 R_e. The orbital period is 57 hours [*Russell*, 1978]. We used 4-s resolution data. The AMPTE/IRM satellite was launched on August 16, 1984, with a perigee of 557 km and an apogee of 18.83 R_e. The inclination is 28.5° and the orbital period is 44.3 hours. The data from AMPTE/IRM were obtained from the three-dimensional (3-D) plasma instrument and the fluxgate magnetometer. We used 4-s resolution data. Further details of these instruments are described by *Paschmann et al.* [1985] and *Lühr et al.* [1985]. The GOES series of geosynchronous meteorological satellites have two-axis magnetometers which measured the vector magnetic field at a 6.6 R_e geosynchronous orbit by taking advantage of spacecraft spin.

Figure 1. Graphical representation of equation (1). The radial distance r varies with r_0 and α. The top panel shows fixed α ($= 0.5$) and variable r_0. The bottom panel shows fixed r_0 ($= 10\ R_e$) and variable α. Note that $R = \sqrt{Y_{GSE}^2 + Z_{GSE}^2} = \sqrt{Y_{GSM}^2 + Z_{GSM}^2}$, which is independent of GSE and GSM coordinates.

We used data from the period January 1978 to December 1986 [*Rufenach et al.*, 1989]. The IMP 8 satellite was launched on October 26, 1973, in an orbit covering a region from 25 R_e to 45 R_e. Its initial orbit was more elliptical than intended, and its eccentricity decreased after launch. Its orbital inclination varied between 0° and about 55° with a periodicity of several years. The data from IMP 8, with 5-min resolution, were averaged from higher resolution data by the National Space Science Data Center (NSSDC). The ISEE 3 satellite provided nearly continuous solar wind measurements in an orbit covering a region from 200 R_e to 260 R_e upstream of the Earth until August 1983. Note that the IMP 8 and ISEE 3 data we used in the present study were normalized to a uniform density calibration independent of ion temperature and velocity [*Petrinec and Russell*, 1993b].

The criterion that the magnetic field undergoes a sudden change in strength or direction, such as when crossing the magnetopause current layer, has been used to identify magnetopause crossings [*Berchem and Russell*, 1982; *Paschmann et al.*, 1986; *Song et al.*, 1988]. This criterion is good for identifying crossings which have a large magnetic shear at the magnetopause. Large shear at the dayside magnetopause usually accompanies southward IMF conditions. However, in this study in some situations, for example, for northward IMF, the field rotation was less than 20° and the field magnitude changed very little. It was hard to identify this kind of low-shear crossing using magnetometer data alone. Therefore, the plasma data were also used for identification. Low-shear crossings have been studied by *Russell and Elphic* [1978] and *Paschmann et al.* [1978, 1993]. A total of 860 crossings were obtained using these identification criteria. Note that all of these crossings are from separate passes. If multiple crossings occur within an hour, the innermost crossing was chosen. Multiple magnetopause crossings are usually caused by the magnetopause oscillation corresponding to upstream variations. Many of the crossings are detected when the magnetopause moves from one equilibrium position to another and therefore do not represent the equilibrium position. Under these circumstances, we have chosen to use the innermost crossing to represent the pass. However, we note the the possibility that the magnetopause may oscillate around its equilibrium due to some instabilities such as Kelvin-Helmholtz instability. The percentage of multiple-crossing passes is only 13%, so there is little difference between using the innermost crossing and using the median crossing.

Since the magnetopause size and shape changes with variations in solar wind conditions, we need to know the solar wind condition for each individual crossing. The solar wind data from IMP 8 and ISEE 3 were used to specify the solar wind conditions during magnetopause crossings observed by ISEE 1 and 2 and AMPTE/IRM. We note that for much of IMP 8's lifetime, there was no solar wind measurement available when IMP 8 crossed the magnetopause. Since we only use data from IMP 8 for $X > 0$, where $X = X_{GSM} = X_{GSE}$ is the position of

IMP 8 in a Sun-Earth direction, IMP 8 is always sunward of the Earth for these crossings. The time lag for the solar wind flowing from IMP 8 or ISEE 3 to the magnetopause has been taken to be 10 min for IMP 8 and 55 min for ISEE 3. Using 5-min-average data, the possible time lags for the IMP 8 data are 0, 5, 10, 15, and 20 min. Therefore, we chose 10 minutes as an average time lag. The data from IMP 8 were first used to examine solar wind conditions. If a data gap occurred or if IMP 8 was not in the solar wind, the data from ISEE 3 were used. Since the data from ISEE 1 and 2, AMPTE/IRM, and IMP 8 may have biases caused by the apogee of their orbits, we only used the crossings from positions $X \geq -6$ R_e for ISEE 1 and 2 and AMPTE/IRM, and $X \geq -32$ R_e for IMP 8. Moreover, we only used the crossings which had both corresponding solar wind plasma and magnetic data. Under these restrictions, there were 553 crossings available for our statistical study. There are 282 crossings from ISEE 1, 235 crossings from ISEE 2, 15 crossings from AMPTE/IRM, and 21 crossings from IMP 8.

The interplanetary control variables, D_p and B_z, for these 553 crossings are plotted in Figure 2. The average value of D_p is 1.915 nPa and the average value of B_z is −0.595 nT. The solid elliptic curve in Figure 2 contains 92% of entire data set. Six percent of the entire data set is in the area between the solid and dotted curves. The uncertainty is smaller in the area inside the solid curve. The uncertainty is larger in the area between the solid and dotted curves. Outside the dotted curve, the number of data points is not sufficient to obtain r_0 and α.
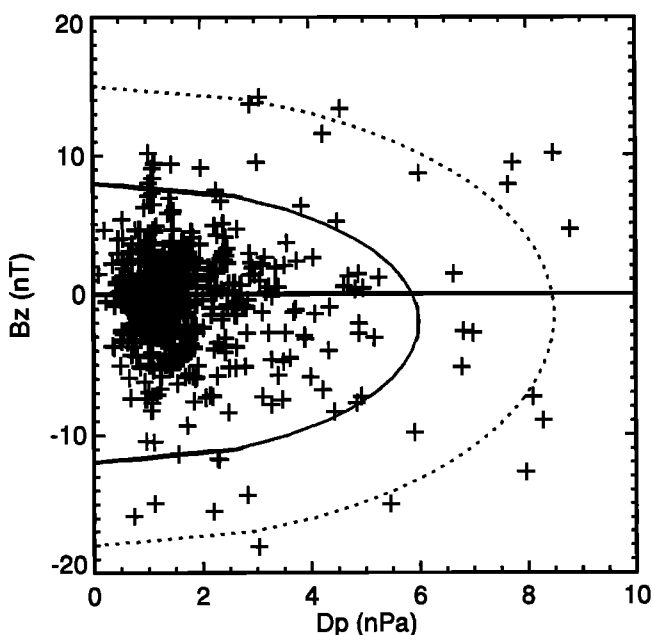

Figure 2. The interplanetary control variables, D_p and B_z, for each individual crossing. The solid elliptic curve encloses 92% of the entire data set. The area between the solid and dotted curves contains 6% of the entire data set.

The motion of the Earth around the Sun causes an aberration or apparent rotation of the direction of flow and hence of the positions of magnetopause crossings. The solar wind aberration has been corrected by a rotation of angle $\theta_{aberr} = \tan^{-1} V_{es}/V_{sw}$, where V_{es} is the velocity of Earth around Sun (30 km/s), and V_{sw} is the velocity of the solar wind. Axial symmetry has been assumed in this study. The magnetopause size and shape have been expressed in the aberrated distance perpendicular to the Earth-Sun line $R = \sqrt{Y_{GSE}^2 + Z_{GSE}^2} = \sqrt{Y_{GSM}^2 + Z_{GSM}^2}$, where R is independent of GSE and GSM coordinates. If the magnetopause is not cylindrically symmetric, the cross section we obtain will be most appropriate near the equatorial region where the data were principally acquired.

3. Determination of $r_0(B_z, D_p)$ and $\alpha(B_z, D_p)$

From (1), the radial distance, r, is characterized by r_0 and α. We have examined the dependence of r_0 and α on various solar wind parameters, specifically, IMF B_x, B_y, and B_z; clock angle; cone angle; and D_p. We found that r_0 and α are significantly affected by only B_z and D_p. In this section we will discuss how to obtain the functional forms of r_0 and α in terms of B_z and D_p.

Our objective is to obtain a function to best describe these measurements. The scheme of linear least squares fitting has been used to accomplish this objective. However, since (1) is a nonlinear function, we cannot use it directly . By taking the natural logarithm of both sides of the equation, (1) can be rewritten in a linear form for later use. We have

$$\ln(r) = -\alpha \ln(1 + \cos\theta) + A \qquad (2)$$

where

$$A = \ln(r_0) + \alpha \ln(2). \qquad (3)$$

The terms $\ln(r)$ and $\ln(1 + \cos\theta)$ are the variables to be fit, and the coefficients α and A are the slope and the intersect of the fitting line. Equation (3) can be rewritten as

$$r_0 = \exp^{A - \alpha \ln(2)} \qquad (4)$$

The position for each individual crossing has been transformed to the forms $\ln(r)$ and $\ln(1 + \cos\theta)$, and then plotted in the top panel of Figure 3. The data points show a linear tendency. We applied a linear least squares fit to these points, and obtained $\alpha = 0.612$ and $A = 2.743$. Using (4), we calculated $r_0 = 10.161 R_e$, as noted in the bottom panel of Figure 3. Knowing r_0 and α, we can derive the size and shape of the magnetopause from (1) and plot it as the solid line in the bottom panel of Figure 3. The standard deviation is defined by $\sqrt{\sum(r_i - r_i')^2}/\sqrt{N}$, where r_i is the observation, r_i' is the calculation, and N is the total number of data points. The probable error of the best-fit value is estimated by the standard deviation over the square root of the total number of data points, that
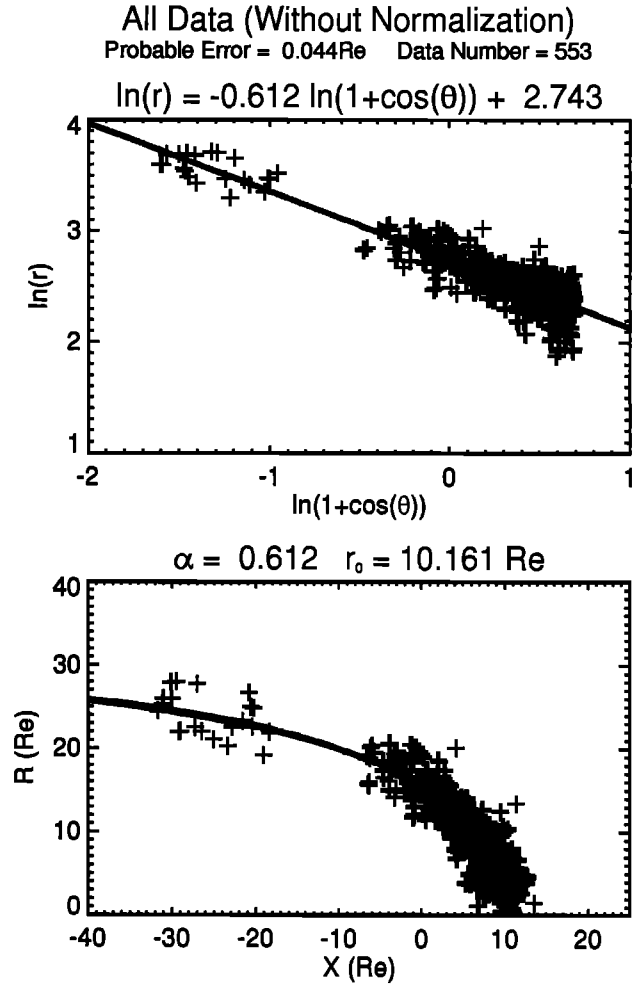

All Data (Without Normalization)
Probable Error = 0.044Re   Data Number = 553

$$\ln(r) = -0.612 \ln(1+\cos(\theta)) + 2.743$$

$$\alpha = 0.612 \quad r_0 = 10.161 \text{ Re}$$

Figure 3. Comparison of the observed points and fitted curves. This figure is for all the data without any normalization. The top panel shows the least squares fitting in $\ln(r)$ and $\ln(1 + \cos\theta)$ space. This result can be transformed to real X and R space, as shown in the bottom panel. The solid line represents the size and shape of the magnetopause.

is, $\sqrt{\sum(r_i - r_i')^2}/N$. The probable error of the best-fit value in this case is 0.044 R_e. Note that there is an important physical difference between the probable error of best-fit value and the standard deviation. The more times we sample, the better we know the best-fit value. However, the standard deviation of the samples about the best-fit value will remain the same no matter how often we sample.

In order to determine how the magnetopause size and shape varies with different solar wind parameters, we need to allow each parameter to vary independently. Since these conditions rarely exist in nature, there is much scatter in the data. To reduce the scatter, the data should be normalized to the same conditions. As mentioned previously, the size and shape of the magnetopause depends mainly on B_z and D_p. We will discuss the B_z effect on magnetopause size and shape by normalizing the data to the average D_p and discuss the D_p

effect on magnetopause size and shape by normalizing the data to the average B_z.

The location of the magnetopause is determined by pressure balance between the solar wind dynamic pressure, D_p, and the pressure of the geomagnetic field, $B^2/2\mu_0$, where μ_0 is the permeability of free space. It is expected that the subsolar magnetopause location, r_0, varies as the one-sixth root of the D_p [*Schield*, 1969]:

$$r_0 = k(D_p)^{-\frac{1}{6}} \qquad (5)$$

where k is a constant of proportionality. To normalize the data to the average value of D_p, we calculate the adjustment amount δr_0 of the standoff point determined from the average D_p ($= 1.915$ nPa) value and from the corresponding D_p value for each individual crossing using (5). If the D_p value is greater than the average D_p value, δr_0 is positive, and vice versa. The amount of δr_0 is traced back along $\alpha = 0.612$ (assuming the magnetopause is self-similar, and α is calculated from a linear fit in Figure 3) to calculate the adjustment amount δr at the location of a crossing. We add δr to the observed r and obtain a normalized r which corresponds to the average D_p. The same procedure used for producing
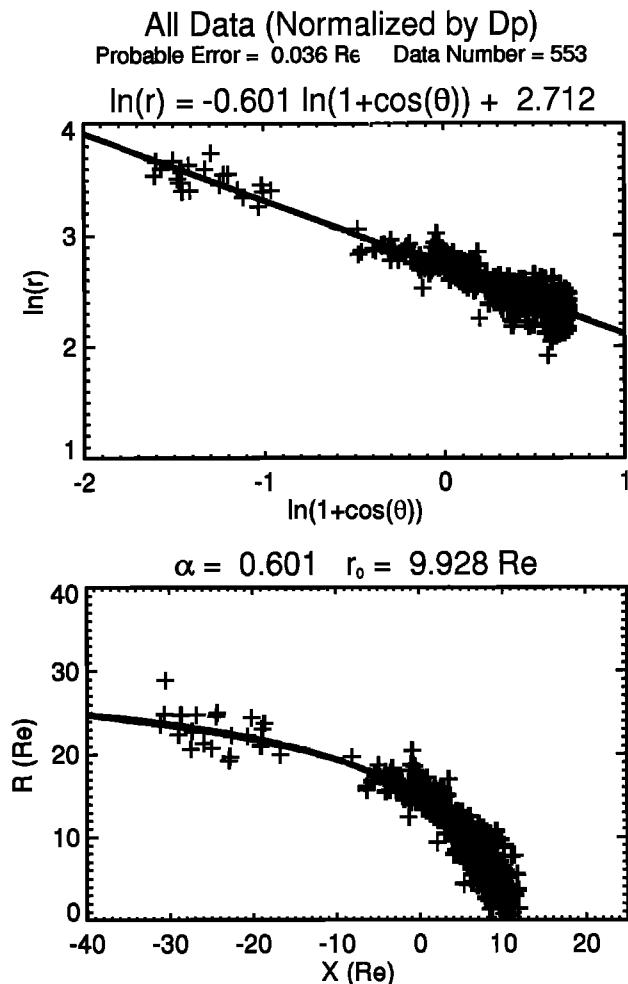

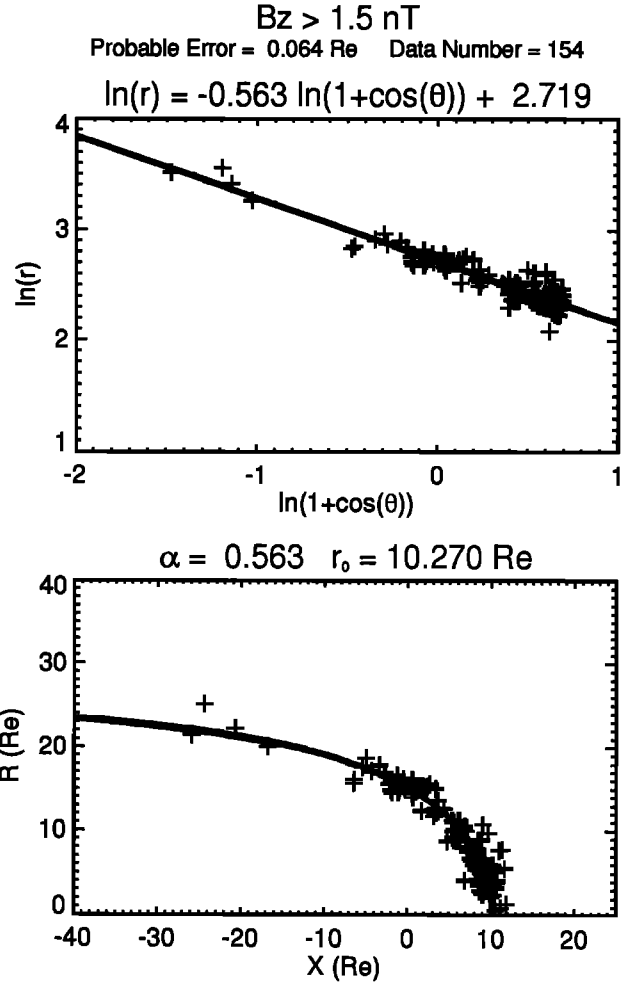**Figure 4.** The same format as Figure 3, but for all the data with normalization by D_p.

Figure 5. The same format as Figure 3, but for northward IMF data with normalization by D_p.

Figure 3 was applied to the normalized data and plotted in Figure 4. The scatter of the data is reduced, and the probable error of the best-fit value decreases from 0.044 R_e to 0.036 R_e.

The normalized data were separated into three bins on the basis of the orientation of the IMF; northward IMF ($B_z \geq 1.5$ nT), horizontal IMF (-1.5 nT $\leq B_z <$ 1.5 nT), and southward IMF ($B_z < -1.5$ nT). The data in each bin have been processed and plotted in the same format as Figure 3. Figure 5 shows the northward IMF case. In this case the probable error of the best-fit value is 0.064 R_e, α is 0.563, and r_0 is 10.270 R_e. When the IMF is in the horizontal direction, as shown in Figure 6, the standoff distance and α do not change much. This suggests that there is no reconnection process occurring, and no magnetic flux removed from the dayside to the nightside for the cases of northward and horizontal IMF. However, both r_0 and α show significant changes when the IMF is southward, as shown in Figure 7. The best-fit value of r_0 changes from 10.270 R_e to 9.451 R_e and α changes from 0.563 to 0.651. As mentioned previously, a larger α means larger flaring in the tail. This implies that some magnetic flux has been transferred

-1.5 nT < Bz < 1.5 nT
Probable Error = 0.058 Re   Data Number = 201

$$\ln(r) = -0.585 \ln(1+\cos(\theta)) + 2.723$$

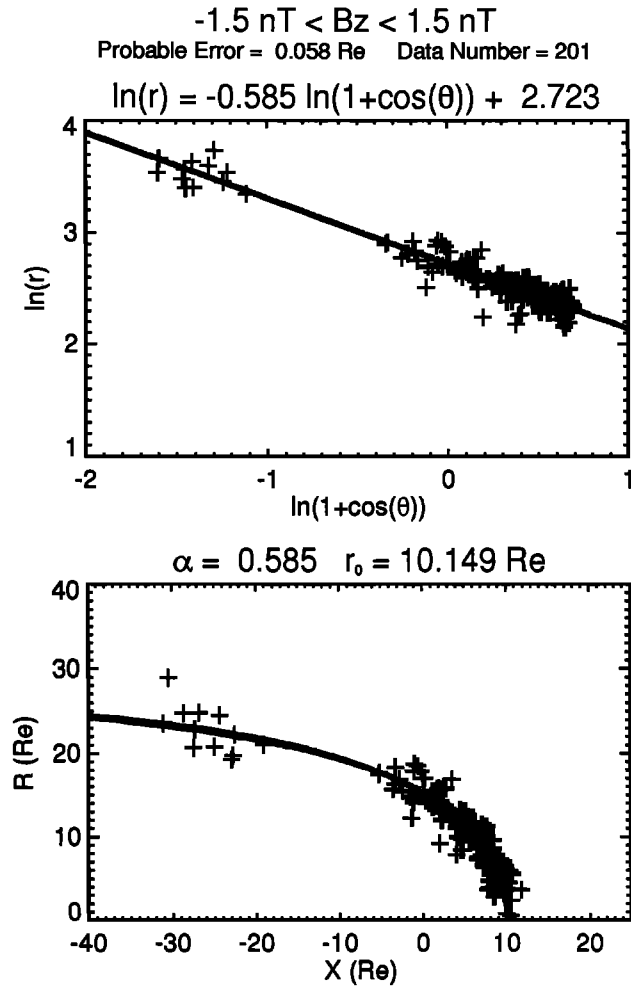$$\alpha = 0.585 \quad r_0 = 10.149 \text{ Re}$$

Figure 6.   The same format as Figure 3, but for horizontal IMF data with normalization by D_p.

to nightside. This feature is consistent with the results of *Petrinec et al.* [1991], *Petrinec and Russell* [1993a, 1996], and *Roelof and Sibeck* [1993].

Petrinec and Russell [1993a, 1996] limit their discussion to the range from −10 to 10 nT, and *Roelof and Sibeck* [1993] limit their results from −7 nT to 7 nT (IMF B_z). In this study we provide a formula for a greater range of B_z, as indicated in Figure 2. The data have been separated into 34 overlapping bins, from −18 nT to 15 nT, which are 6 nT wide and are shifted by 1 nT. The data in each bin have been processed by the same procedure used for producing Figure 3. We determine r_0 and α for each bin representing a specific value of IMF B_z. For bins in the ranges −18 nT < B_z < −12 nT and 8 nT < B_z < 15 nT, there are few data points. However, these data points are distributed evenly over local time, and we still can obtain a reasonable r_0 and α. Outside the range −18 nT < B_z < 15 nT, the parameter α becomes unreasonable. Figure 8 shows how r_0 and α vary with IMF B_z. The diamond symbol with an error bar represents the best-fit value and probable error of the best-fit value for each bin. The number indicated above or below each error bar shows the number of data

points in each bin. The variation of r_0, as shown in the top panel of Figure 8, can be represented as two linear portions with a break at $B_z = 0$ nT. The linear least squares fits have been applied separately to the points on either side of $B_z = 0$ nT. The slopes of the right and left lines are 0.013 and 0.131, respectively. The best-fit value of r_0 decreases when the value of southward IMF increases. This implies that the more the southward IMF, the more magnetic flux is removed from the subsolar region. Therefore, tail flaring increases proportionally to the flux lost at the subsolar region. As shown in the bottom panel of Figure 8, the best-fit value of α, which has been fit to one line, decreases with a slope of 0.011 when the IMF B_z increases. We can write the fitting results in the following form:

$$r_0 = \begin{cases} 10.150 + 0.013B_z, & \text{for } B_z \geq 0 \\ 10.146 + 0.131B_z, & \text{for } B_z < 0 \end{cases} \quad (6)$$

$$\alpha = 0.590 - 0.011B_z. \quad (7)$$

Note that (6) and (7) only apply for $D_p = 1.915$ nPa, the average D_p for all crossings. The associated errors for (6) are 0.160 R_e for $B_z \geq 0$ and 0.155 R_e for $B_z < 0$. The associated error for (7) is 0.039.
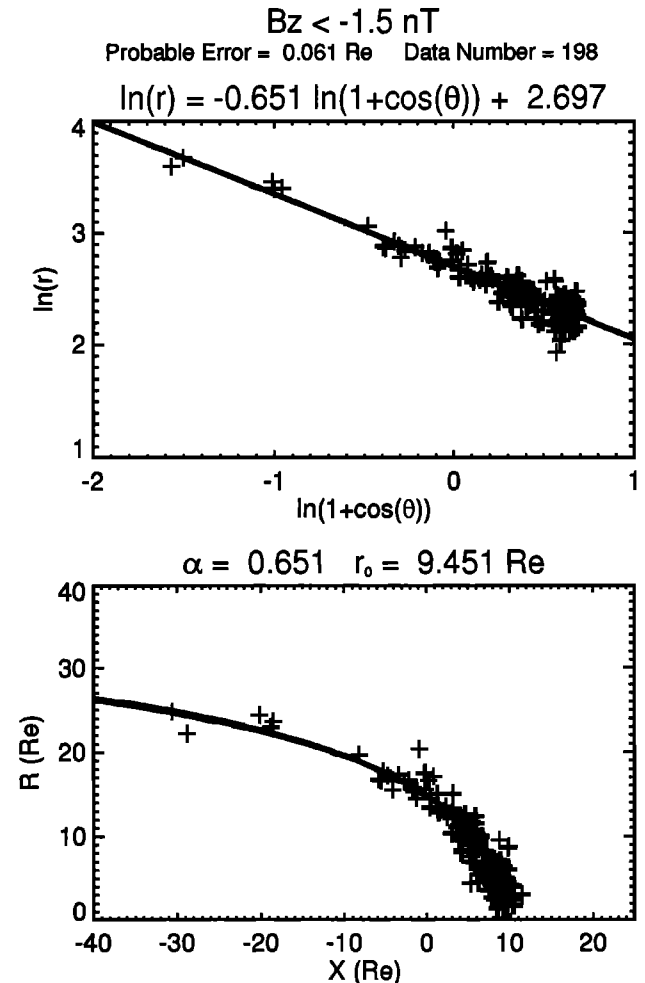
Bz < -1.5 nT
Probable Error = 0.061 Re   Data Number = 198

$$\ln(r) = -0.651 \ln(1+\cos(\theta)) + 2.697$$

$$\alpha = 0.651 \quad r_0 = 9.451 \text{ Re}$$

Figure 7.   The same format as Figure 3, but for southward IMF data with normalization by D_p.

magnetosheath as a magnetopause crossing. This error would cause the radial distance of the magnetopause to be abnormally large. Moreover, r_0 is also different in Figures 8 and 9 for $B_z < 5$ nT. The time resolution of the solar wind measurements used to normalize the data sets may contribute to this discrepancy. *Roelof and Sibeck* [1993] used a 1-hour average of solar wind data sets, whereas we used 5-min resolution. Thus, several 1-hour intervals which average to a small positive value of IMF B_z may actually have been southward during the period of time that the magnetopause was crossed. The same argument can be applied to intervals which average to small southward values of IMF B_z. Therefore, hourly averages of solar wind parameters will blur the trends in the magnetopause standoff distance for northward and southward IMF conditions. In our study the overlapping bins may also blur the response of the magnetopause position to weak northward and southward IMF. However, we represent all the data points as two
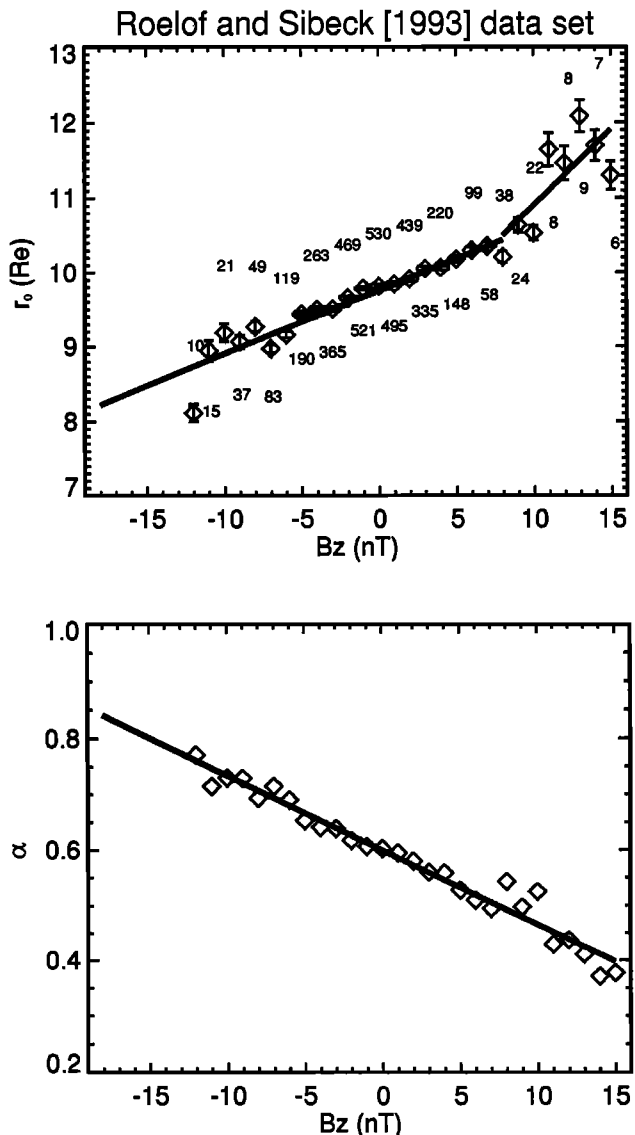

Figure 8. The variation of r_0 and α with B_z. This relation is for $D_p = 1.915$ nPa. The diamond symbols represent the best-fit values of r_0 and α. The error bar shows the probable error of the best-fit value. The solid lines show the fits. The number indicated above or below each error bar shows the number of data points for each bin.

We now apply the same procedure to the entire *Roelof and Sibeck* [1993] data set. The results are shown in Figure 9. These results are strikingly different from our results. The best-fit value of r_0 increases linearly until $B_z = 8$ nT and then increases sharply for larger values of northward IMF (Note that *Roelof and Sibeck* [1993] did not discuss the range $B_z > 7$ nT). We believe their data set contains several difficulties. First, their data were compiled by different investigators using different criteria. Thus it is not a homogeneous data set. Second, the magnetic fields on both sides of the magnetopause were in the same direction when the IMF was northward. If the investigations did not use plasma data to aid in identifying the crossing, their procedure risks identifying a discontinuity convected through the

Figure 9. The same format as Figure 8, but using *Roelof and Sibeck* [1993] data.

All Data (Normalized by Bz)
Probable Error = 0.043 Re Data Number = 553

$$\ln(r) = -0.606 \ln(1+\cos(\theta)) + 2.759$$

[plot: ln(r) vs ln(1+cos(θ))]

α = 0.606 r_o = 10.367 Re

[plot: R (Re) vs X (Re)]
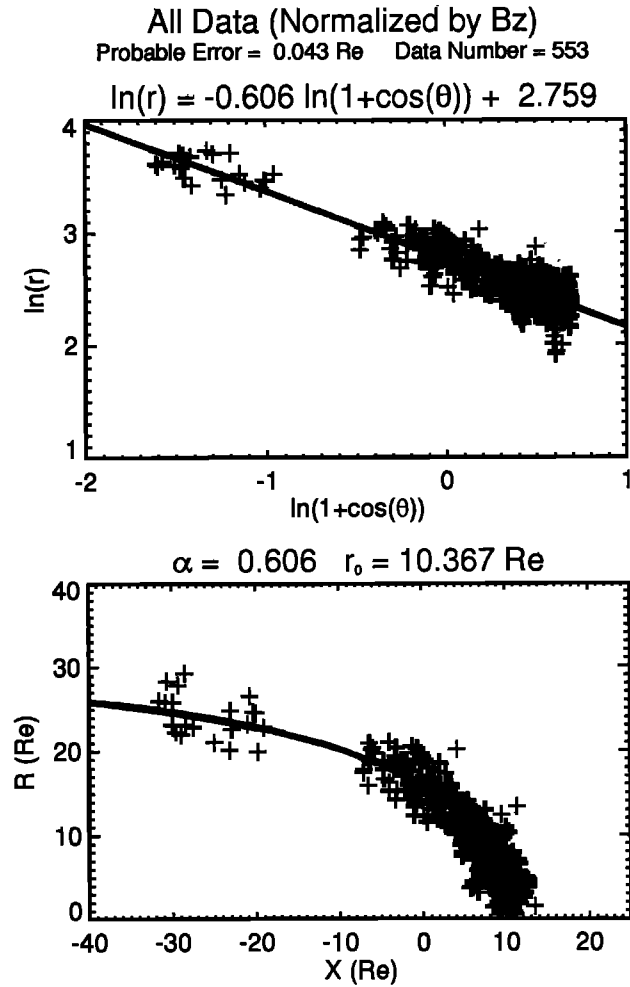
Figure 10. The same format as Figure 3, but for all the data with normalization by B_z.

ble error of the best-fit value to 0.043 R_e, as shown in Figure 10. These normalized data have been divided into three bins on the basis of the value of D_p, $D_p \geq$ 2.5 nPa, 1.5 nPa $\leq D_p <$ 2.5 nPa, and $D_p <$ 1.5 nPa, and the results are plotted in Figures 11-13. Comparing the best-fit values of r_0 and α in these figures, we find that the best-fit value of α increases slightly with increasing D_p and that the best-fit value of r_0 increases when D_p decreases. These results imply that D_p also has a role in flux transfer from the dayside to the nightside. To further understand this relation, the data have been separated into 17 overlapping bins, from 0.5 nPa to 8.5 nPa, which are 4 nPa wide and are shifted by 0.5 nPa. For bins in the range 6 nPa $< D_p <$ 8.5 nPa, there are few data points. However, these data points distribute evenly over local time, and we still can obtain reasonable values for r_0 and α. Outside the range of 0.5 nPa $< D_p <$ 8.5 nPa, α is unreasonable. The best-fit values of r_0 and α for each bin are plotted in Figure 14. The best-fit value of r_0 has a power law of $-1/6.6$ with respect to D_p, which is slightly different from the $-1/6$ theoretical prediction. A linear trend for α has a 0.010 slope. The fitting results for $B_z = -0.595$ nT can be written as follows:
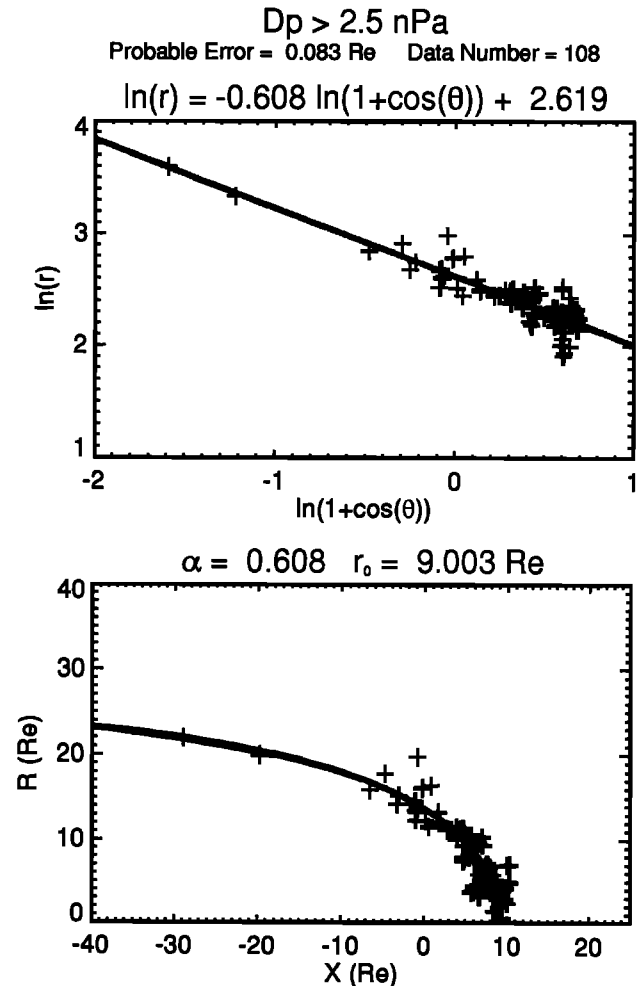
linear portions with a break in the slope at $B_z = 0$ nT. The slopes of the two portions have been determined by using a multiple parameter fit at the last stage of this fitting procedure. Also, the data set from *Sibeck et al.* [1991] and *Roelof and Sibeck* [1993] used crossings from spacecraft both in and outside of the equatorial plane. *Sibeck et al.* [1991] show a figure which illustrates different magnetopause locations in the equatorial plane and in the noon-midnight meridian plane. Asymmetries due to the cusp could also contribute to the discrepancies.

Using the data set constructed for the study in this paper, we have shown how r_0 and α change with IMF B_z. Now we want to see how these two parameters vary with D_p. In a manner similar to our earlier analysis, the data need to be normalized to the same value of IMF B_z, -0.595 nT (the average B_z for all crossings). We can obtain r_0 and α from (6) and (7) for a given B_z and then the location of the magnetopause. Therefore, we can calculate δr between the locations for the average B_z and for each individual crossing (each crossing has a corresponding B_z) at a specific θ. We add δr to observed r and obtain a normalized r which corresponds to the average B_z. This procedure reduces the proba-

Dp > 2.5 nPa
Probable Error = 0.083 Re Data Number = 108

$$\ln(r) = -0.608 \ln(1+\cos(\theta)) + 2.619$$

[plot: ln(r) vs ln(1+cos(θ))]

α = 0.608 r_o = 9.003 Re

[plot: R (Re) vs X (Re)]

Figure 11. The same format as Figure 3, but for large D_p with normalization by B_z.

1.5 nPa < Dp < 2.5 nPa
Probable Error = 0.065 Re   Data Number = 145

$$\ln(r) = -0.601 \ln(1+\cos(\theta)) + 2.716$$
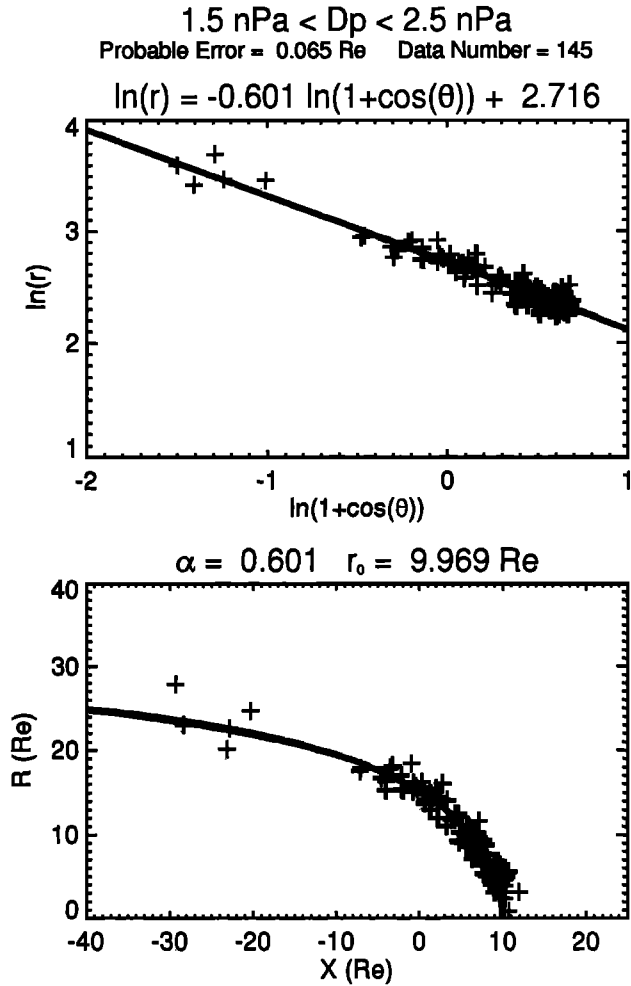

$\alpha = 0.601$ $r_0 = 9.969$ Re

Figure 12. The same format as Figure 3, but for intermediate D_p with normalization by B_z.

$$r_0 = kD_p^{-\frac{1}{6.6}}, \tag{8}$$

$$\alpha = 0.572 + 0.010D_p, \tag{9}$$

where k is a constant of proportionality. The associated errors for (8) and (9) are 0.422 R_e and 0.032, respectively. Although the exponential form for the magnetopause standoff distance as a function of solar wind dynamic pressure is the most physically reasonable model, the fit actually intersects very few of the best-fit values (including error bars). This is due to a large number of data points in large bins, leading to a very small probable error of the best-fit value, which is much smaller than the standard deviation.

4. Multiple Parameter Fitting

In the previous section the effect of dynamic pressure on the magnetopause size and shape was obtained by normalizing the crossing data for the effect of B_z. Similarly, the effect of B_z on the magnetopause location was obtained by normalizing the data for the dynamic pressure. In this section we will consider the effect of B_z and

D_p simultaneously by using a multiple parameter fitting technique. We have used a gradient search nonlinear optimization technique [Bevington, 1969; Khurana and Kivelson, 1994] to obtain the least squares solution. The technique predicts the locations of the magnetopause crossings by following the gradient of the root mean square difference in the parameter space. Since the functional form for the relationship between the dependent variable (magnetopause location) and the independent variables (B_z and D_p) is known, we can combine (6)-(9) to obtain

$$r_0 = \begin{cases} (a_1 + a_2B_z)(D_p)^{-\frac{1}{a_4}}, & \text{for } B_z \geq 0 \\ (a_1 + a_3B_z)(D_p)^{-\frac{1}{a_4}}, & \text{for } B_z < 0 \end{cases} \tag{10}$$

$$\alpha = (a_5 + a_6B_z)(1 + a_7D_p), \tag{11}$$

where parameters a_1 through a_7 are to be optimized by using the gradient search technique. Note that the work of previous sections is necessary to obtain the form of (10) and (11). The initial seed values of these parameters are shown in the first column of Table 1. We have added a factor of 1.16 to the proton's dynamic pressure
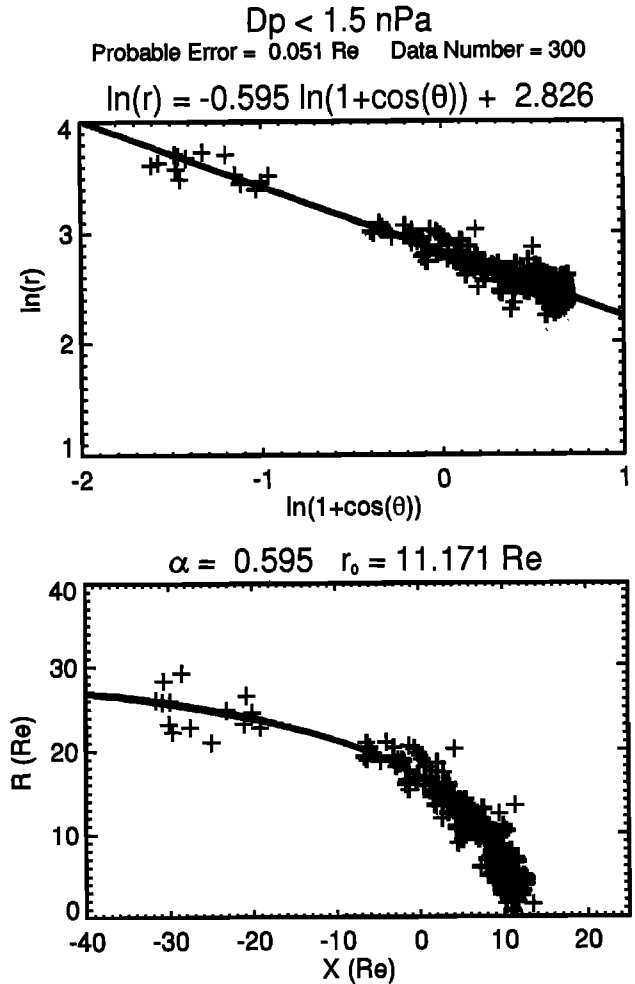
Dp < 1.5 nPa
Probable Error = 0.051 Re   Data Number = 300

$$\ln(r) = -0.595 \ln(1+\cos(\theta)) + 2.826$$

$\alpha = 0.595$ $r_0 = 11.171$ Re

Figure 13. The same format as Figure 3, but for small D_p with normalization by B_z.

Table 1. The Coefficients of Equations (10) and (11) Before and After the Multiple Parameters Fit

	Before Fit	After Fit
a_1	10.2	11.4 $\pm$ 0.2
a_2	0.013	0.013$\pm$ 0.001
a_3	0.13	0.14 $\pm$ 0.01
a_4	6.6	6.6 $\pm$ 0.8
a_5	0.59	0.58 $\pm$ 0.02
a_6	-0.011	-0.010$\pm$ 0.002
a_7	0.010	0.010$\pm$ 0.001

The right column shows the coefficients before the fit; and the left column shows the coefficients with their uncertainties after the fit.

1.97 R_e to 1.24 R_e after we apply the multiple parameter fit. Equations (10) and (11) can now be rewritten as

$$r_0 = \begin{cases} (11.4 + 0.013B_z)(D_p)^{-\frac{1}{6.6}}, & \text{for } B_z \geq 0 \\ (11.4 + 0.14B_z)(D_p)^{-\frac{1}{6.6}}, & \text{for } B_z < 0 \end{cases} \quad (12)$$

$$\alpha = (0.58 - 0.010B_z)(1 + 0.010D_p), \quad (13)$$

The dependence of r_0 and α on the solar wind parameters B_z and the logarithm of D_p can be illustrated graphically by using contour and surface plots. Figure 16 shows r_0 and Figure 17 shows α. The asterisks in the bottom panel of Figure 16 show magnetopause crossings at geosynchronous orbit taken from Table 1 of *Rufenach et al.* [1989]. Five-minute resolution observa-
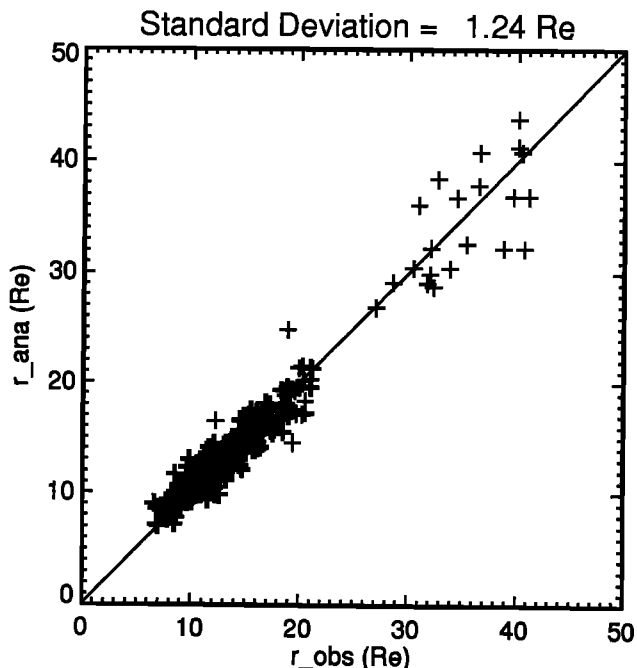
Figure 14. The variation of r_0 and α with D_p. This relation is for $B_z = -0.595$ nT. The diamond symbols represent the best-fit value of r_0 and α. The error bar shows the probable error of the best-fit value. The solid lines show the fits. The number indicated above or below each error bar shows the number of data points for each bin.

to reflect the contribution from the solar wind helium content. Neglecting the helium content will cause the magnetopause location to be overestimated by 2.5%. The final optimized values and uncertainties are shown in the second column of the table. The uncertainty of each coefficient is obtained by the Monte Carlo simulation method. The multiple parameter fittings have been run 200 times using one third of the total points, which are sampled randomly each time. We obtain 200 sets of coefficients and take their standard deviations as their uncertainties. The comparison between the analytic and the observed radial locations of the magnetopause are shown in Figure 15. The solid line has a slope of 1. The data points are distributed evenly around the solid line. The standard deviation between the analytic and the observed values is improved from

Figure 15. The comparison between the observed and the analytic radial distances. The solid line represents where both the observed and the analytic values are the same.
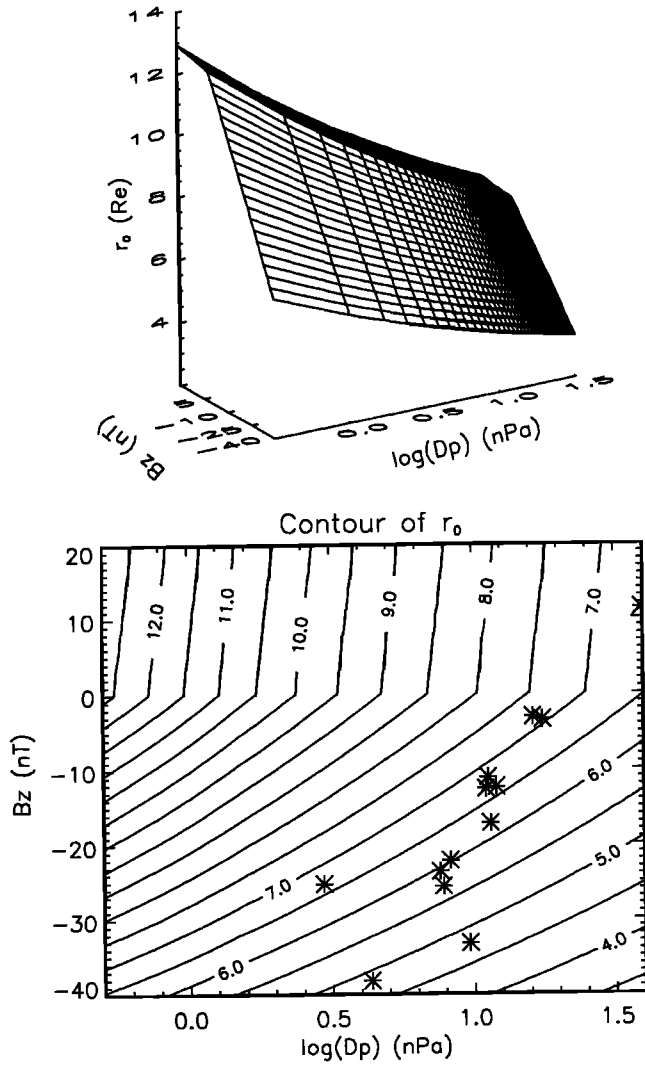
netopause moves earthward and tail flaring increases when the IMF is southward. Also, the size and shape of the magnetopause is not self-similar for various solar wind dynamic pressure when the IMF is northward. However, as discussed below, there are some differences between our model and the others.

Figure 18 shows a comparison with the *Petrinec et al.* [1991] model. *Petrinec et al.* [1991] only divided the data which were normalized by $D_p = 2$ nPa, into southward and northward bins. In comparison to their results, we chose $D_p = 1.915$ nPa and $B_z = 2.856$ nT for northward IMF, and $B_z = -3.403$ nT for southward IMF. We obtained these values by averaging the corresponding B_z values for the northward and southward IMF bins, respectively. The solid curves in Figure 18 represent the size and shape of the magnetopause from the present study, and the dotted lines show the size and shape from their model. It can be seen that our results are very consistent with their results only on the dayside. Since they fit the data to an elliptic form, this
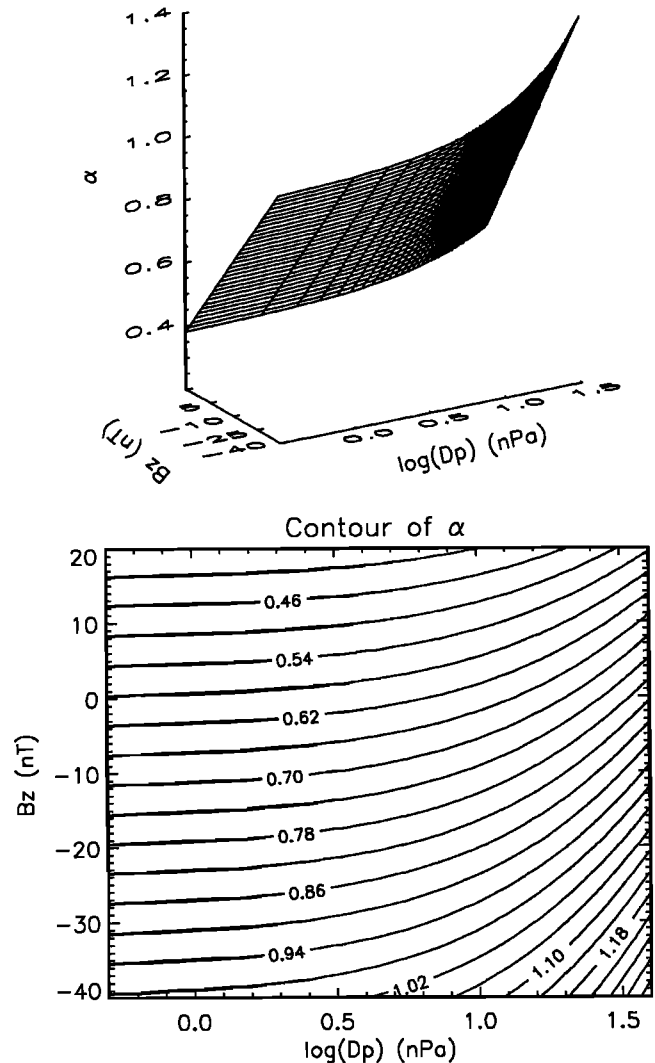

Figure 16. Surface and contour plots for r_0 as a function of B_z and $\log(D_p)$. The contour interval is 0.5 R_e. The star signs show the GOES crossings at 6.6 R_e.

tions of corresponding D_p and B_z were available for 13 of 64 crossings. This confirms the observation of *Rufenach et al.* [1989] that the magnetopause moved inside of the geosynchronous orbit on the dayside when both D_p and southward IMF were large. This plot also illustrates the difficulty of using data obtained at geosynchronous orbit in such analyses. Clearly, for some of the crossings, the magnetopause was in transition from outside to inside geosynchronous orbit. While it was observed at 6.6 R_e, its equilibrium position, appropriate to the B_z and D_p recorded in the solar wind, was not reached until later. Inclusion of such points as crossings at 6.6 R_e will adversely bias statistics of magnetopause crossings.

5. Comparisons With Previous Models

In this section we compare our results with models developed by *Petrinec et al.* [1991], *Petrinec and Russell* [1993a, 1996], and *Roelof and Sibeck* [1993]. All these models and ours have confirmed that the dayside mag-

Figure 17. Surface and contour plots for α as a function of B_z and $\log(D_p)$. The contour interval is 0.04.

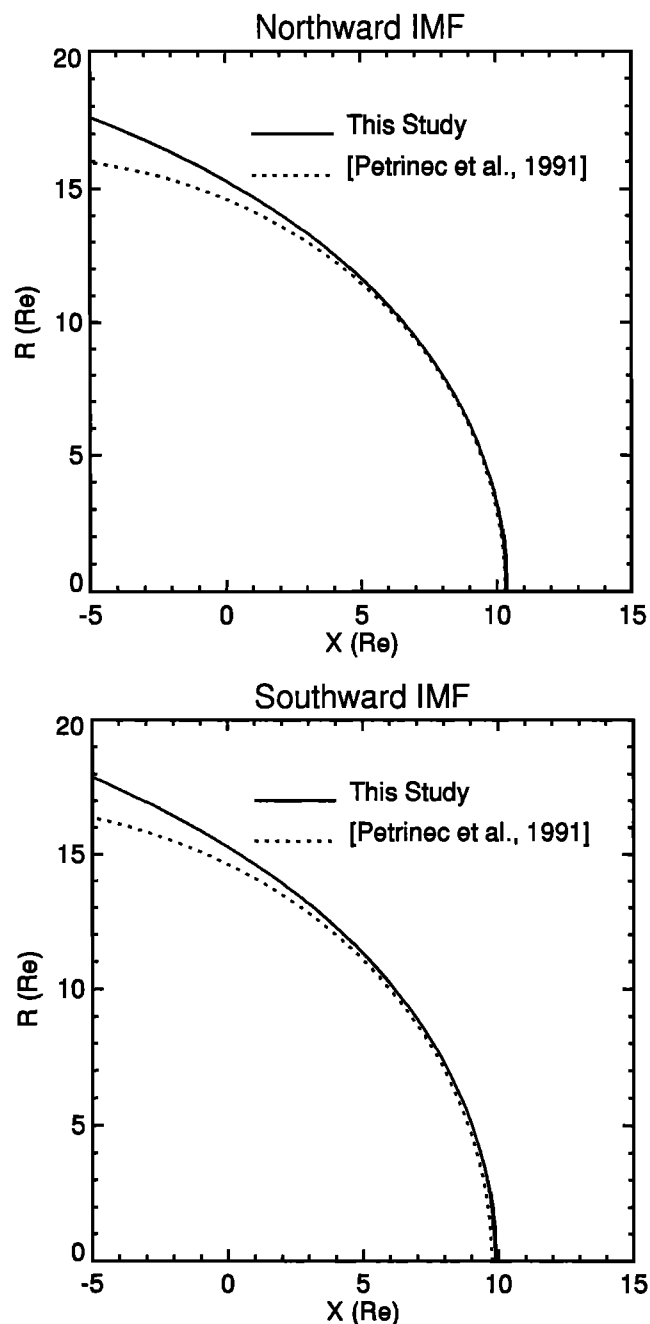## Northward IMF

Southward IMF

Figure 18. Comparison of the results of this paper with the size and shape of the magnetopause of *Petrinec et al.* [1991]. The solid line shows the size and shape of the magnetopause from the present study, and the dotted line shows the size and shape of the magnetopause from *Petrinec et al.* [1991].

may cause the curve to bend close to Earth in the region of $-5\ R_e < X < 0\ R_e$. Thus the size and shape results in a smaller nose radius.

The size and shape of the magnetopause on the nightside is more variable than that on the dayside. *Petrinec and Russell* [1993a, 1996] studied the size and shape of the magnetotail $(-10\ R_e \geq X \geq 22.5\ R_e)$ depending on different B_z and D_p. Their results are shown in bottom panel of Figure 19. They showed three curves

for $B_z \geq 0$ nT, $B_z = -5$ nT, and $B_z = -10$ nT for three different values of D_p. They showed no dependence on northward B_z. We have plotted our results in the same format as theirs in the top panel of Figure 19. We find that our three curves intersect with each other (at $-12\ R_e$ for $D_p = 0.5$ nPa, at $-10\ R_e$ for $D_p = 2$ nPa, and at $-6\ R_e$ for $D_p = 8$ nPa), and the position of the intersecting point depends on D_p. Our tail radii are typically smaller than theirs, and the difference between ours and theirs is the largest for the case when $D_p = 0.5$ nPa. *Petrinec and Russell* [1993a] has a similar convergence of solutions at the terminator as ours. Their dependence on D_p is stronger than this model's. Note that they used data determined from the pressure balance between the solar wind and magnetosphere and not directly from in situ magnetopause measurements.

Roelof and Sibeck [1993] also studied the size and shape of the magnetopause covering both dayside and nightside and for various IMF B_z and D_p conditions. The equation they used is an ellipse. An ellipse must close at some point in the tail, thus it cannot represent a magnetopause that continues to flare. Their results were shown in Figure 9 of their paper. For comparison with their results, we chose two cases which are similar to theirs (rows 1 and 4 in Figure 20) and another two cases which are different from theirs (rows 2 and 3 in Figure 20). The left column is produced using this model and the right column is from theirs. The *Roelof and Sibeck* [1993] model shows that the magnetotail flaring for different B_z values depends strongly on D_p. Also the flaring varies with D_p when the IMF is northward. In the present study the flaring changes slightly with D_p for northward and southward IMF B_z.

6. Conclusions

This study provides another look at the fitting of the magnetopause size and shape which is independent of *Petrinec et al.* [1991], *Petrinec and Russell* [1993a, 1996], and *Roelof and Sibeck* [1993]. We have used crossings from ISEE 1 and 2, AMPTE/IRM, and IMP 8 satellites, which we identified using consistent criteria, and fit in a new functional form which is characterized by two parameters, r_0 and α. The parameters r_0 and α represent the balance between the solar wind dynamic pressure and the magnetic pressure of the Earth's dipole field, and the level of flaring, respectively. The parameters r_0 and α are controlled by the IMF B_z and D_p. To obtain the initial relations, we normalized the data by the average D_p or B_z and binned the data using a range of B_z or D_p conditions. Then we used a multiple parameter fit to determine the coefficients for r_0 and α as a function of B_z and D_p. The final form of the fit with coefficients for the size and shape of the magnetopause is given in (1), (12), and (13). These equations have some general features; for example, the magnetopause moves inward when the IMF is southward, and the standoff distance increases very slightly when the northward IMF increases. For the tail region, the flaring becomes larger when the IMF is southward, which is
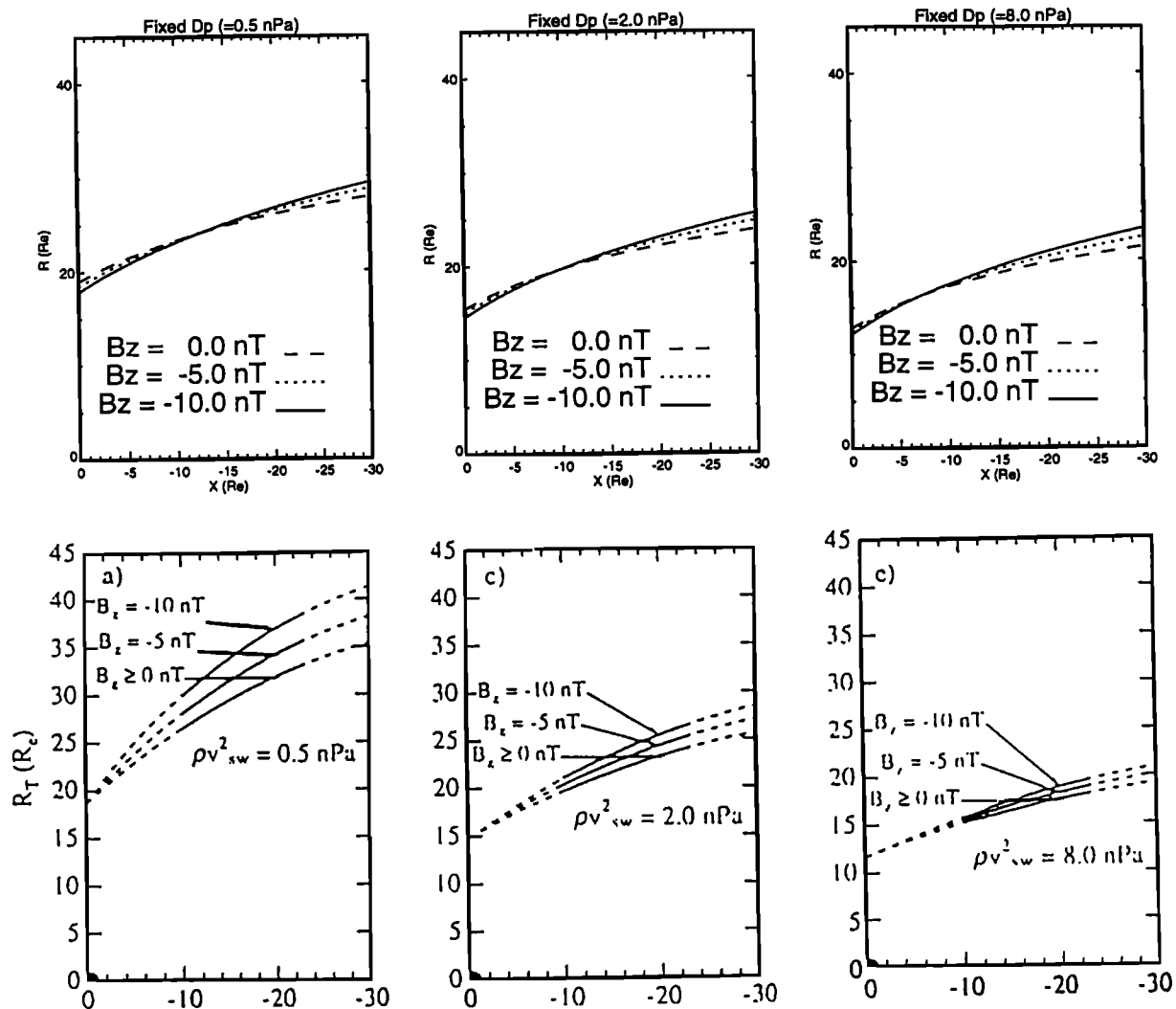
Figure 19. Comparison of the results of this paper (top panel) with Figure 4 of *Petrinec and Russell* [1993a] (bottom panel). Three cases are chosen for comparison: fixed $D_p = 0.5$ nPa, 2.0 nPa, and 8.0 nPa.

generally believed to be caused by reconnection at the dayside removing magnetic flux to the nightside. Also the flaring of the magnetopause increases slightly as D_p increases.

Moreover, we obtain a power law of $-1/(6.6 \pm 0.8)$ for r_0 versus D_p. The theoretical prediction is $-1/6$ for a perfect dipole in a vacuum, which is within the error range. Some variation in this value may be due to the thermal pressure interior to the magnetosphere. Another possible cause for the variation is associated with neglecting of the static pressure (especially magnetic pressure) in the solar wind. When the solar wind has a small dynamic pressure but a large magnetic pressure, the values of the standoff distance may actually correspond to a higher total pressure of the solar wind, and the effect is to move the power law curve closer to $-1/6$. However, we have examined the real solar wind measurements in our data set, and the difference between the dynamic and magnetic pressures is about 2 orders of magnitude. We also have added the mag-

netic pressure into the total pressure and recalculated the power law. The power law remains unchanged.

Petrinec et al. [1991] and *Petrinec and Russell* [1993a] used two separate functional forms to represent the size and shape of the magnetopause at both dayside and nightside locations, but the form derived in this paper is a single functional form which eliminates the flaring angle discontinuity across the terminator. Furthermore, our model is an explicit expression in a simple conic form. This formula is useful for operational space applications such as predicting when satellites at geosynchronous orbit will find themselves in the magnetosheath.

Determining the size and shape of the magnetopause in the tail is a very difficult problem. Several factors influence the magnetopause position, and these influences become more important at further distances downtail from the Earth. The most notable of these influences are the exact (rather than average) angle of the solar wind flow vector with respect to the Sun-Earth line;
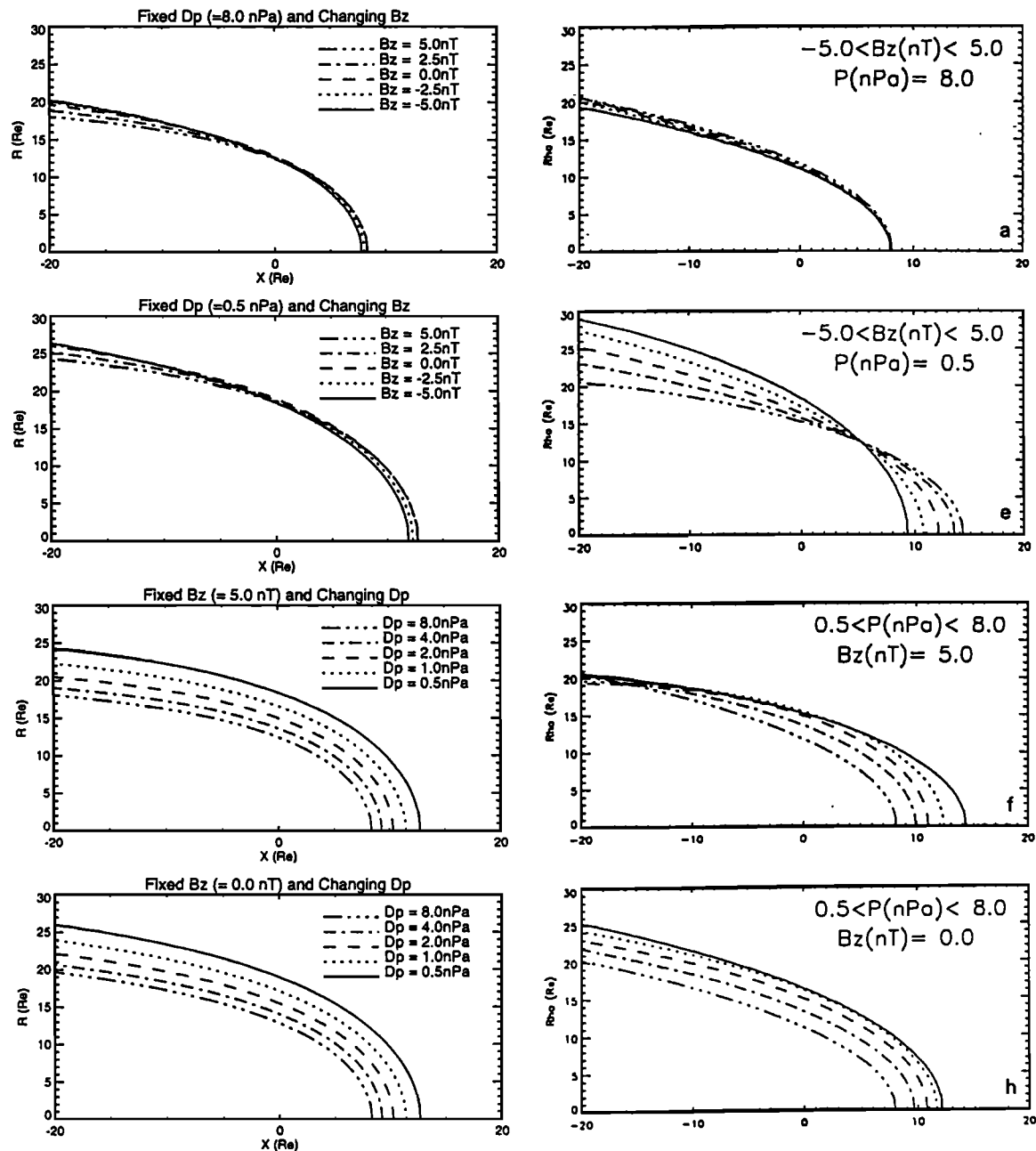
Figure 20. Comparison of the results of this paper (left) with Figure 9 of *Roelof and Sibeck* [1993] (right). The different line styles represent different values of D_p and B_z, as indicated in the legend.

the dipole tilt angle of the Earth (asymmetries in the tail cross section that may result); the static pressure of the solar wind; and dynamic processes internal to the magnetotail (i.e., substorm phase). The error in our magnetopause model may be larger when we extend it further downtail. In our study there are only 21 data points beyond $X = -10\ R_e$ because of many data gaps in the IMP 8 data and the corresponding solar wind data from ISEE 3 is limited. In spite of these limitations, our model seems to fit the data very well, as illustrated in Figures 5-7 which show the fit for different IMF B_z conditions normalized by dynamic pressure

and in Figures 11-13 which show the fit for different dynamic pressure normalized by IMF B_z.

The comparisons with previous models serve to show how different data sets, with different assumptions, and different functional forms can lead to very different dependencies of the magnetopause size and shape on solar wind parameters. Also, the size and shape of the magnetopause is uncertain at extreme values of the IMF B_z and solar wind dynamic pressure. The magnetopause size and shape cannot be determined with more certainty until additional data sets are available from future missions.

References

Berchem J., and C. T. Russell, The thickness of the magnetopause current layer: ISEE 1 and 2 observations, *J. Geophys. Res.*, *87*, 2108, 1982.

Bevington, P. R., *Data Reduction and Error Analysis for the Physical Sciences*, McGraw-Hill, New York, 1969.

Fairfield, D. H., Average and unusual locations of the Earth's magnetopause and bow shock, *J. Geophys. Res.*, *76*, 6700, 1971.

Fairfield, D.H., Observations of the shape and location of the magnetopause: A review, in *Physics of the Magnetopause, Geophys. Monogr. Ser.*, vol. 90, edited by P. Song, B.U.Ö. Sonnerup, and M.F.Thomsen, pp.53, AGU, Washington D. C., 1995.

Formisano, V., V. Domingo, and K. -P. Wenzel, The three-dimensional shape of the magnetopause, *Planet. Space Sci.*, *27*, 1137, 1979.

Howe, H. C., and J. H. Binsack, Explorer 33 and 35 plasma observations of magnetosheath flow, *J. Geophys. Res.*, *77*, 3334, 1972.

Khurana, K. K., and M. G. Kivelson, A variable cross-section model of the bow shock of Venus, *J. Geophys. Res.*, *99*, 8505, 1994.

Lühr, H., N. Klöcker, W. Oelschlägel, B. Häusler, and M. Acuña, The IRM fluxgate magnetometer, *IEEE Trans. Geosci. Remote Sens.*, *23*, 259, 1985.

Paschmann, G., N. Sckopke, G. Haerendel, I. Papamastorakis, S. J. Bame, J. R. Asbridge, J. T. Gosling, E. W. Hones Jr., and E. R. Tech, ISEE plasma observations near the subsolar magnetopause, *Space Sci. Rev.*, *22*, 717, 1978.

Paschmann, G., H. Loidl, P. Obermayer, M. Ertl, R. Laborenz, N. Sckopke, W. Baumjohann, C. W. Carlson, and D. W. Curtis, The plasma instrument for AMPTE/IRM, *IEEE Trans. Geosci. Remote Sens.*, *23*, 262, 1985.

Paschmann, G, I. Papamastorakis, W. Baumjohann, N. Sckopke, C. W. Carlson, B. U. Ö. Sonnerup, and H. Lühr, The magnetopause for large magnetic shear: AMPTE/IRM observations, *J. Geophys. Res.*, *91*, 11,099, 1986.

Paschmann, G, W. Baumjohann, N. Sckopke, and T. D. Phan, Structure of the dayside magnetopause for low magnetic shear, *J. Geophys. Res.*, *98*, 13,409, 1993.

Petrinec, S. M., and C. T. Russell, An empirical model of the size and shape of the near-Earth magnetotail, *Geophys. Res. Lett.*, *20*, 2695, 1993a.

Petrinec, S. M., and C. T. Russell, The intercalibration of solar wind instruments during the International Magnetospheric Study, *J. Geophys. Res.*, *98*, 18,963, 1993b.

Petrinec, S. M., and C. T. Russell, Near-Earth magnetotail shape and size as determined from the magnetopause flaring angle, *J. Geophys. Res.*, *101*, 137, 1996.

Petrinec, S. M., P. Song, and C. T. Russell, Solar cycle variations in the size and shape of the magnetopause, *J. Geophys. Res.*, *96*, 7893, 1991.

Roelof, E. C., and D. G. Sibeck, Magnetopause shape as a bivariate function of interplanetary magnetic field B_z and solar wind dynamic pressure, *J. Geophys. Res.*, *98*, 21,421, 1993. (Correction, *J. Geophys. Res.*, *99*, 8787, 1994.)

Rufenach, C. L., R. F. Martin, Jr., and H. H. Sauer, A study of geosynchronous magnetopause crossings, *J. Geophys. Res.*, *94*, 15,125, 1989.

Russell, C. T., The ISEE 1 and 2 fluxgate magnetometers, *IEEE Trans. Geosci. Electron.*, *16*, 239, 1978.

Russell, C. T., and R. C. Elphic, Initial ISEE magnetometer results: Magnetopause observations, *Space Sci. Rev.*, *22*, 681, 1978.

Schield, M. A., Pressure balance between solar wind and magnetosphere, *J. Geophys. Res*, *74*, 1275, 1969.

Sibeck, D. G., R. E. Lopez, and E. C. Roelof, Solar wind control of the magnetopause shape, location, and motion, *J. Geophys. Res.*, *96*, 5489, 1991.

Song, P., R. C. Elphic, and C. T. Russell, ISEE 1 & 2 observations of the oscillating magnetopause, *Geophys. Res. Lett.*, *15*, 744, 1988.

J. K. Chao and H. C. Fu, Institute of Space Science, National Central University, Chungli, 32054, Taiwan. (e-mail: T272362@twncu865.ncu.edu.tw; hcfu@sedc.ss.ncu.edu.tw)

K. K. Khurana and C. T. Russell, Institute of Geophysics and Planetary Physics, University of California, Los Angeles, 6877 Slichter Hall, Los Angeles, CA 90095-1567. (e-mail: kkhurana@igpp.ucla.edu; ctrussel@igpp.ucla.edu)

J.-H. Shue, Solar-Terrestrial Environment Laboratory, Nagoya University, Honohara 3-13, Toyokawa, Aichi 442, Japan. (e-mail: jhshue@stelab.nagoya-u.ac.jp)

Howard J. Singer, NOAA R/E/SE, Space Environment Center, 325 Broadway, Boulder, CO 80303-3328. (e-mail: hsinger@sec.noaa.gov)

P. Song, Space Physics Research Laboratory, The University of Michigan, 2455 Hayward Street, Ann Arbor, MI 48109-2143. (e-mail: psong@umich.edu)